RMetS
Royal Meteorological Society

Long-range transport of Saharan dust and its radiative impact on precipitation forecast: a case study during the Convective and Orographically-induced Precipitation Study (COPS)

Jean-Pierre Chaboureau,[a]* Evelyne Richard,[a] Jean-Pierre Pinty,[a] Cyrille Flamant,[b] Paolo Di Girolamo,[c] Christoph Kiemle,[d] Andreas Behrendt,[e] Hélène Chepfer,[f] Marjolaine Chiriaco[b] and Volker Wulfmeyer[e]

[a]*Laboratoire d'Aérologie, Université de Toulouse and CNRS, Toulouse, France*
[b]*Laboratoire Atmosphères, Milieux et Observations Spatiales, Université Pierre et Marie Curie and CNRS, Paris, France*
[c]*Dipartimento di Ingegneria e Fisica dell'Ambiente, Università degli Studi della Basilicata, Potenza, Italy*
[d]*Institut für Physik der Atmosphäre, Deutsches Zentrum für Luft- und Raumfahrt, Oberpfaffenhofen, Germany*
[e]*Institut für Physik und Meteorologie, Universität Hohenheim, Stuttgart, Germany*
[f]*Laboratoire de Météorologie Dynamique, Institut Pierre-Simon Laplace, Université Pierre et Marie Curie, Paris, France*
*Correspondence to: J.-P. Chaboureau, Laboratoire d'Aérologie, Observatoire Midi-Pyrénées, 14 av. Belin, F-31400 Toulouse, France. E-mail: jean-pierre.chaboureau@aero.obs-mip.fr

A Saharan dust event affected the Rhine valley in southwestern Germany and eastern France on 1 August 2007 during the Convective and Orographically-induced Precipitation Study (COPS) experiment. Prior to an episode of intense convection, a layer of dry, clean air capped by a moist, dusty layer was observed using Cloud-Aerosol Lidar and Infrared Pathfinder Satellite Observation (CALIPSO) and airborne and ground-based lidar observations from North Africa to western Europe. The origin of the different layers was investigated using the regional model Meso-NH. For the purpose of modelling evaluation, a lidar simulator was developed for direct comparison of observed and simulated vertical structures of the lidar backscattered signal. Overall, the model reproduced the vertical structure of dust probed several times by the different lidar systems during its long-range transport. From Lagrangian back trajectories it was found that the dust was mobilized from sources in Mauritania six days earlier, while the dry layer subsided over the north Atlantic. Off the Moroccan coasts, the dry layer folded down beneath the dusty air mass and the two-layer structure was advected to the Rhine valley in about two days. By heating the atmosphere, the dust layer changed the static stability of the atmosphere and thus the occurrence of convection. A study of sensitivity to the radiative effect of dust showed a better prediction of precipitation when a dust prognostic scheme was used rather than climatology or when dust effects were ignored. This result suggests that dust episodes that occur prior to convective events might be important for quantitative precipitation forecasts. Copyright © **2011 Royal Meteorological Society**

Key Words: convective precipitation; mesoscale modelling

Received 11 February 2010; Revised 12 July 2010; Accepted 29 September 2010; Published online in Wiley Online Library 2 February 2011

Citation: Chaboureau J-P, Richard E Pinty J-P, Flamant C, Di Girolamo P, Kiemle C, Behrendt A, Chepfer H, Chiriaco M, Wulfmeyer V. 2011. Long-range transport of Saharan dust and its radiative impact on precipitation forecast: a case study during the Convective and Orographically-induced Precipitation Study (COPS). *Q. J. R. Meteorol. Soc.* **137**: 236–251. DOI:10.1002/qj.719

1. Introduction

Long-range transport of mineral dust in the free troposphere is important in many aspects including radiative transfer, cloud microphysics, atmospheric chemistry, oceanic biogeochemical processes and air quality. Dust from the deserts of North Africa, the largest sources of dust in the world, occasionally affects Europe (Ansmann *et al.*, 2003; Kishcha *et al.*,

Copyright © 2011 Royal Meteorological Society

2007) and the Mediterranean up to 8 km altitude (Alpert *et al.*, 2004). Dust outbreaks that reach western Europe occur mainly during the warm season from late spring to early autumn, as probed by lidar systems during the period May 2000–December 2002 (Papayannis *et al.*, 2008). This generally happens with synoptic conditions characterized by the presence of a high-pressure region over Libya and a trough over the Bay of Biscay (e.g. Moulin *et al.*, 1998; Barkan *et al.*, 2005; Kallos *et al.*, 2006). The trough leads to northeastward advection of warm air and convective destabilization downstream of the trough, while the high pressure favours mobilization of dust over Chad and the western Sahara. The radiative impact of dust is of importance, as the warm flow accompanied by high dust load can cause warming of the order of 6–8 K at 700 hPa compared with normal conditions (Barkan *et al.*, 2005).

Such a change in thermal structure can affect the skill of forecasts that do not predict dust routinely. This issue has been investigated in a few studies using regional models allowing online interaction of dust load with radiation, and consequently with the model dynamics. For example, Pérez *et al.* (2006) found that the use of an interactive dust-radiation model improved the temperature forecasts over dust-affected areas during a major dust outbreak in the Mediterranean. Chaboureau *et al.* (2007) showed an improvement in the capture of the observed convective activity over West Africa in the two-day range with the use of prognostic dust. More recently, Heinold *et al.* (2008) found dust radiative feedback on Saharan boundary-layer dynamics and dust mobilization. However, the radiative impact on quantitative precipitation forecasts has received little attention so far.

From June–August 2007, the international field campaign called the Convective and Orographically-induced Precipitation Study (COPS: Wulfmeyer *et al.*, 2008) took place in southwestern Germany and eastern France. The goal of COPS was to advance the quality of forecasts of orographically induced convective precipitation by four-dimensional observations and modelling of its life cycle. Here, we focus on a line of thunderstorms that triggered on the afternoon of 1 August 2007 over southwestern France. Prior to this convective episode, several ground-based lidars observed a dust layer reaching the COPS area. The dust layer was also seen from airborne lidars in both the COPS area and upstream, over the Iberian Peninsula and France. Some days before, Cloud-Aerosol Lidar and Infrared Pathfinder Satellite Observation (CALIPSO) observations probed the dust layer off the Moroccan coasts. The long-range transport of this dust event was investigated using a mesoscale model, Meso-NH (Lafore *et al.*, 1998).

For evaluation purposes, a lidar simulator was developed by adopting the so-called model-to-satellite approach. This approach consists of calculating any remotely sensed radiative quantities from the predicted model fields, allowing a direct comparison with coincident observations from satellite or other platforms. It offers the advantage that the satellite data are used without being combined with any ancillary data, thus avoiding the possible impact of inconsistent assumptions between simulated and retrieved geophysical fields. This approach was first used in Meso-NH to identify discrepancies of cloud-cover forecasts using infrared observations from geostationary satellites (Chaboureau *et al.*, 2000, 2002). It thus allowed a statistical assessment of long series of cloud forecasts (Chaboureau and Bechtold, 2005; Chaboureau and Pinty, 2006; Söhne *et al.*, 2008). Complementary studies using microwave observations further assessed the cloud scheme (Wiedner *et al.*, 2004; Meirold-Mautner *et al.*, 2007; Chaboureau *et al.*, 2008). Following the same approach, other instrument emulators were implemented into the Meso-NH system to simulate precipitation radar products (Richard *et al.*, 2003; Caumont *et al.*, 2006) and GPS zenithal delay (Brenot *et al.*, 2006; Yan *et al.*, 2009). The lidar simulator presented here is able to take account of the radiative impact of all the scattering particles predicted by the model, including cloud droplets, ice crystals, dust and other aerosol particles. It is flexible enough to follow the assumptions made about the particle distributions by the different microphysical schemes developed within Meso-NH. It also handles the different wavelengths and viewing geometries operating in the lidar systems.

Here, this approach is used to evaluate the ability of the Meso-NH model to simulate the transport of dust from the Sahara to western Europe. The aim of this study is threefold: first, to assess the Saharan origin of the dust event; second, to bring out the benefit of the lidar simulator for evaluating the vertical structure of the aerosol fields; third, to examine the impact of the dust-generated temperature perturbation on the precipitation forecast. In a first step, the vertical distribution and optical thickness of the dust, which were simulated with a run nudged towards analysis, were assessed. In a second step, sensitivity runs showed the positive impact of the dust-induced temperature perturbation in quantitative precipitation forecasts over France. Only the radiative effect of dust was taken into account. No interaction between aerosol and cloud was considered here.

This article is organized as follows. Section 2 describes the model and experimental design, the lidar simulator and the lidar observations. Section 3 details the long-range transport of dust. Section 4 gives a quantitative evaluation of the simulated profiles of the lidar signal and water vapour. Section 5 presents the radiative impact of the Saharan dust on precipitation forecasts through a study of sensitivity to different representations of dust. Section 6 concludes the article.

2. Model and lidar observations

2.1. Model description

The numerical simulations were performed with the non-hydrostatic mesoscale model Meso-NH (Lafore *et al.*, 1998), version 4.7. The two-way interactive grid-nesting method (Stein *et al.*, 2000) enabled the model to be run simultaneously on several domains with the same vertical levels but with different horizontal resolutions. The lateral boundary conditions were given by large-scale European Centre for Medium-Range Weather Forecasts (ECMWF) operational analyses for the outermost model, and they were provided by the outer models for the inner models at every time step. The case was simulated with triply nested models, with a horizontal grid spacing of 32, 8 and 2 km. The vertical grid had 70 levels up to 27 km with a level spacing of 40 m close to the surface to 600 m at high altitude. The simulation domains are shown in Figure 1.

For the two coarser-resolution grids (32 and 8 km), the subgrid scale convection was parametrized by a mass-flux convection scheme (Bechtold *et al.*, 2001). For the inner

Copyright © 2011 Royal Meteorological Society

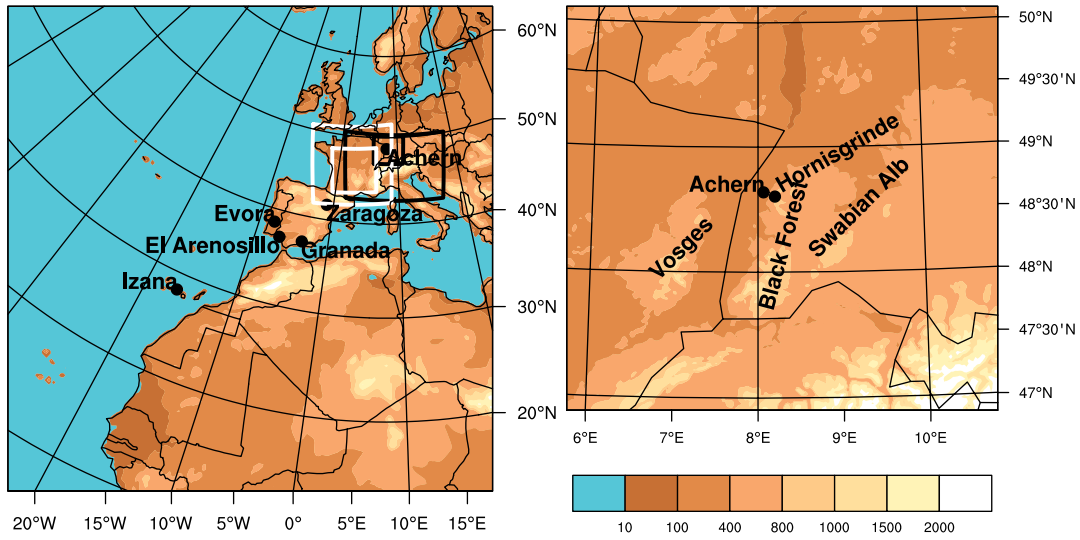

Figure 1. (a) Geographical domains used for the nested forecasts. The outer frame shows the 32 km grid mesh domain and its topography for all the Meso-NH experiments. The location of the 8 and 2 km grid mesh domains for the REF (DUST, NODUST and CLIM) experiment(s) are indicated with the rectangles in black (white). (b) Topography (m) of the 2 km grid mesh domain for REF. The names of the AERONET, meteorological and lidar stations used in this study are also given. This figure is available in colour online at wileyonlinelibrary.com/journal/qj

grid (2 km), explicit deep convection was permitted and the convection scheme was switched off. The microphysical scheme included the three water phases with five species of precipitating and non-precipitating liquid and solid water (Pinty and Jabouille, 1998) and a modified ice-to-snow autoconversion parametrization following Chaboureau and Pinty (2006). Subgrid cloud cover and condensate content were parametrized as a function of the normalized saturation deficit by taking both turbulent and convective contributions into account (Chaboureau and Bechtold, 2002, 2005). The turbulence parametrization was based on a 1.5-order closure (Cuxart *et al.*, 2000). The surface-energy exchanges are represented according to the four possible surface-type patches (natural land surfaces, urban areas, ocean, lake) included in a grid mesh. The Interactions between Soil, Biosphere and Atmosphere (ISBA) scheme (Noilhan and Planton, 1989) was used for natural land surfaces. The radiative scheme was the one used at ECMWF (Gregory *et al.*, 2000) including the Rapid Radiative Transfer Model (RRTM) parametrization (Mlawer *et al.*, 1997) for long-wave radiation and the two-stream formulation originally employed by Fouquart and Bonnel (1986) for short-wave radiation. Effects on the radiation scheme due to aerosols other than dust were taken into account by using the climatological distribution of Tegen *et al.* (1997). The radiative effect due to dust depends on the numerical experiments that are described in section 2.2.

The dust prognostic scheme is described in Grini *et al.* (2006). In this parametrization, the three log-normal modes are generated and transported by the log-normal aerosol scheme of the ORganic and Inorganic Log-normal Aerosols Model (ORILAM: Tulet *et al.*, 2005). These modes are described by their zeroth, third and sixth moments, with the latter kept constant. Dust fluxes are calculated from wind-friction speeds using the Dust Entrainment and Deposition (DEAD) model (Zender *et al.*, 2003). The initial dust-size distribution contains three modes with median radii of 0.32, 1.73 and 4.33 μm and standard deviations of 1.7, 1.6 and 1.5, respectively as defined by Alfaro and Gomes (2001). Dust loss occurs through sedimentation and rain-out in convective clouds. Regarding the short-wave effect, the refractive index of the dust aerosols was assigned according to that measured over West Africa. Their values, depending on the wavelength calculated over six spectral intervals, are described in Tulet *et al.* (2008).

2.2. *Numerical experiments*

Four Meso-NH simulations were run: a reference simulation to assess the origin of the dust and its vertical distribution and three simulations to test the sensitivity of rain forecasts to the radiative effects of dust. Table I summarizes the differences characterizing the Meso-NH experiments.

The reference case (REF) was initialized on 26 July 2007 at 0000 UTC. In a first step, it was integrated forward for six days using the outer grid only as model spin-up for dust and cloud. In order to keep the simulation close to the meteorological analyses, the simulation was nudged towards the ECMWF analyses with a six-hour relaxation time, so the radiative effect of dust was smoothed out and dust could be considered as a passive tracer here. At 0000 UTC on 1 August 2007 the model was integrated for 24 h using the three nested domains without nudging. The innermost domain was centred over the COPS area in order to describe the small scales of the mountainous orography well (Figure 1, right).

The sensitivity simulations were also performed with triply nested models but, in these cases, with a different location of the inner domains in order to focus on the convective rain event. The runs were initialized on 28 July 2007 at 0000 UTC starting from the REF simulation and were integrated forward for 4.5 days using the outer grid only. Again, the simulations were nudged towards the ECMWF analysis, but above 6 km only. This kept the large-scale forcing close to the analysis, leaving dust to interact radiatively with the atmosphere below 6 km. At 1200 UTC on 1 August 2007, the model was integrated for 12 h using the three nested domains without nudging. This allowed the convection to develop fully into a line of thunderstorms. The DUST simulation integrated the dust prognostic scheme, the NODUST simulation took no dust

Copyright © 2011 Royal Meteorological Society

Table I. Characteristics of the Meso-NH experiments.

Experiment	Initial time (UTC)	Nudging Effects	Free run initial Time (UTC)	Dust representation
REF	26 Jul 0000	Everywhere	1 Aug 0000	Prognostic dust
DUST	28 Jul 0000	Above 6 km	1 Aug 1200	Prognostic dust
NODUST	28 Jul 0000	Above 6 km	1 Aug 1200	No dust effect
CLIM	28 Jul 0000	Above 6 km	1 Aug 1200	Tegen climatology

effects into account and the CLIM simulation used the climatological dust distribution of Tegen *et al.* (1997).

2.3. Lidar simulator

According to Chiriaco *et al.* (2006) among others, the lidar attenuated backscattered (ATB) signal corrected for geometric effects and calibration constant (expressed in $m^{-1}\,sr^{-1}$) at altitude z and wavelength λ is

$$ATB_\lambda(z) = \left[\beta_{\mathrm{mol},\lambda}(z) + \beta_{\mathrm{par},\lambda}(z)\right] \times \exp\left\{-2\int_0^z \left[\alpha_{\mathrm{mol},\lambda}(z) + \eta\alpha_{\mathrm{par},\lambda}(z)\,\mathrm{d}z\right]\right\}, \quad (1)$$

where α is the extinction coefficient (m^{-1}) and β the backscatter coefficient ($m^{-1}\,sr^{-1}$), caused by both air molecules (mol) and aerosols and cloud particles (par). Multiple scattering by cloud particles is taken crudely into account with $\eta = 0.5$ (Platt, 1973).

Following Collis and Russell (1976), the lidar backscatter and extinction coefficients for molecules, $\beta_{\mathrm{mol},\lambda}$ and $\alpha_{\mathrm{mol},\lambda}$ respectively, are

$$\beta_{\mathrm{mol},\lambda} = 5.45 \times 10^{-32} \times \frac{p}{k_B T} \times \left(\frac{\lambda}{0.55}\right)^{-4.09}, \quad (2)$$

$$\alpha_{\mathrm{mol},\lambda} = \frac{8\Pi}{3}\beta_{\mathrm{mol},\lambda}, \quad (3)$$

where T is temperature (K), p is pressure (hPa), k_B is the Boltzmann constant ($1.38 \times 10^{-23}\,J\,K^{-1}$) and wavelength λ is given in μm.

The optical properties of cloud particles and aerosols were integrated over their size distribution, while extinction $Q_{\mathrm{ext},\lambda}$ and backscatter $Q_{\mathrm{back},\lambda}$ efficiencies were computed using the Mie code of Bohren and Huffman (1985) for spheres. Thus, particles were assumed to be spherical, although particle non-sphericity can be an important factor affecting the extinction to backscatter lidar ratio when the coarse mode prevails (Dubovik *et al.*, 2006). Refraction indices of pure water and ice were used for cloud liquid and ice crystals respectively. For consistency with the numerical experiments, the refractive index of mineral dust was taken from Tulet *et al.* (2008), i.e. $1.448–2.92 \times 10^{-3}i$ at 532 nm, $1.44023–1.16 \times 10^{-3}i$ at 730 and 820 nm and $1.41163–1.06 \times 10^{-3}i$ at 1064 nm.

For the two-moment schemes, the integration over the size distribution of the particles $n_{\mathrm{par}}(D,z)$ was performed using an accurate quadrature formula (here Gauss–Hermite for log-normal size distributions of dust) with

$$\alpha_{\mathrm{par},\lambda}(z) = \int_0^\infty \frac{\Pi}{4} D^2 Q_{\mathrm{ext},\lambda}(D) n_{\mathrm{par}}(D,z)\,\mathrm{d}D, \quad (4)$$

$$\beta_{\mathrm{par},\lambda}(z) = \int_0^\infty \frac{\Pi}{4} D^2 Q_{\mathrm{back},\lambda}(D) n_{\mathrm{par}}(D,z)\,\mathrm{d}D. \quad (5)$$

(The Gauss–Laguerre formula is used for γ-size distributions employed in the two-moment microphysical schemes available in Meso-NH.) For single-moment microphysical schemes, such as the one used here, $\alpha_{\mathrm{par},\lambda}$ and $\beta_{\mathrm{par},\lambda}$ were computed taking an effective radius representative of the distribution, consist with those employed for cloud and ice in the radiative scheme.

In each model column, the particle backscatter coefficient $\beta_{\mathrm{par},\lambda}$ and the extinction coefficient $\alpha_{\mathrm{par},\lambda}$ are both cloud particle and aerosol coefficients. They are computed from equations (4) and (5) using the model mixing ratios (and concentrations when available) of cloud particles and aerosols while the lidar backscatter and extinction coefficients for molecules are calculated using the model profiles of air density.

2.4. Lidar observations

The Cloud-Aerosol Lidar with Orthogonal Polarization (CALIOP) is a two-wavelength polarization-sensitive lidar on board the CALIPSO satellite mission. The orbit passing over the dusty layer occurred around 0300 UTC on 29 July 2007 (see the overpass track in Figure 2(b)). From this orbit, the ATB signal at 532 nm was used.

The Water vapour Lidar Experiment in Space (WALES) differential absorption lidar system (Wirth *et al.*, 2009) was deployed on board the Deutsches Zentrum für Luft- und Raumfahrt (DLR) Falcon. The objective of the mission on 1 August 2007 was to document the atmospheric upstream condition of the COPS area off the western coasts of France prior to a convective event that occurred in the late afternoon (Schäfler *et al.*, 2010). The WALES observations used here are those measured at 1064 nm between 0900 and 1100 UTC, when the DLR Falcon flew above the dust layer on its way back from Faro, Portugal to Oberpfaffenhofen, Germany (see the flight track in Figure 4(b)). The ATB signal at 1064 nm and the water-vapour mixing ratio were examined.

The LEANDRE 2 lidar system was operated on 1 August 2007 in the COPS area from an altitude of 5800 m above sea level on board the Service des Avions Français Instrumentés pour la Recherche en Environnement (SAFIRE) Falcon. The track around 1538 UTC (shown in Figure 6) was selected, as the dust plume was probed by the LEANDRE 2 system. Both the ATB signal at 730 nm and the retrieved water-vapour mixing ratio were employed.

The ground-based University of BASilicata Lidar (BASIL) system was operated at Achern, Germany (48.638°N, 8.066°E, 140 m above sea level, see its location in Figure 1(b)) from June–August 2007. BASIL is a Raman lidar sensing the atmosphere at three wavelengths (355, 532 and

Copyright © 2011 Royal Meteorological Society

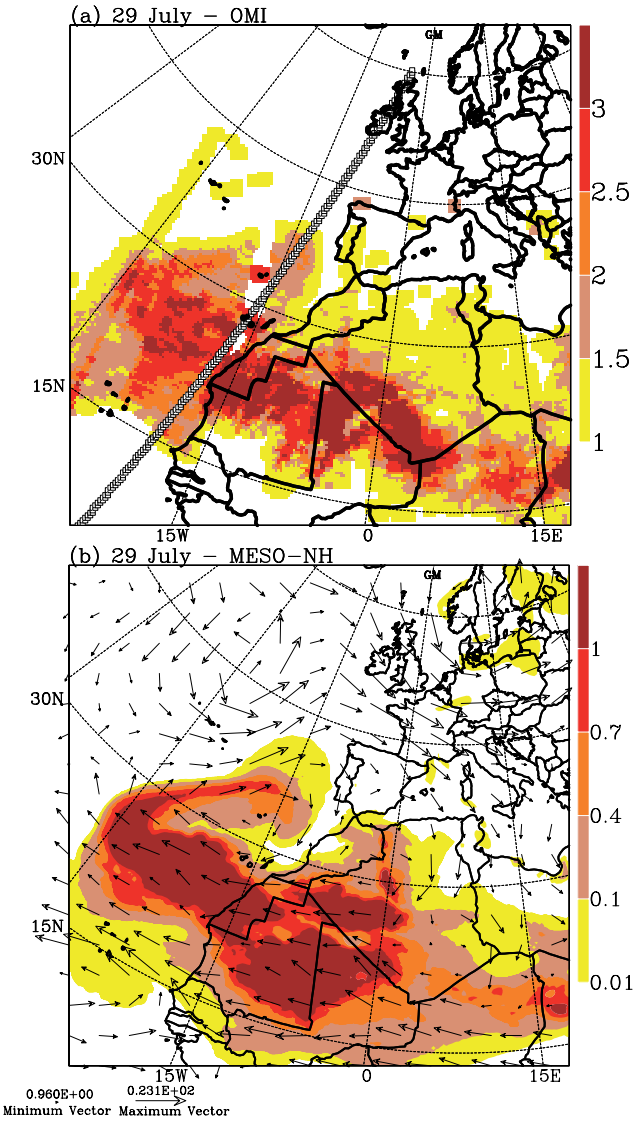

Figure 2. (a) OMI aerosol index and (b) Meso-NH total aerosol burden ($g\,m^{-2}$) at 1200 UTC on 29 July 2007. In (b) the arrows show the 700 hPa wind vectors from Meso-NH. In (a) the line of squares indicates the track of CALIPSO at 0300 UTC on 29 July 2007. The domain is 6400 km long. Longitude and latitude lines are plotted every 15°. This figure is available in colour online at wileyonlinelibrary.com/journal/qj

1064 nm), thus allowing the water-vapour mixing ratio to be measured. BASIL also provides measurements of atmospheric temperature and multiwavelength measurements of particle backscattering, extinction and depolarization (Di Girolamo *et al.*, 2009). The water-vapour mixing ratio was used together with β_{par} at 1064 nm.

The ground-based University of Hohenheim (UHOH) lidar system was operated at Hornisgrinde, Germany (48.604°N, 8.204°E, 1161 m above sea level, see its location in Figure 1(b)) from June–August 2007 (Behrendt *et al.*, 2009). It is a differential absorption lidar system sensing the atmosphere in the near-infrared, around 820 nm, and provides water-vapour number density as its primary measured parameter. In addition to moisture, β_{par} at 820 nm is also measured. Both these data sets were used in the following.

The lidar observations had higher spatial and temporal resolution than the model. In consequence, the lidar observations were averaged and projected on to the Meso-NH grid on which the comparison between observation and simulation was made.

3. Long-range transport of Saharan dust

3.1. *Export of dust out of Africa*

An overview of the dust event on 29 July 2007 is given in Figure 2. The aerosol index (AI) obtained from the Ozone Monitoring Instrument (OMI) (Torres *et al.*, 1998, 2002) is positive for aerosols absorbing at UV wavelengths, such as dust. AI is sensitive to dust load, and to the altitude at which the dust is transported. At UV wavelengths, absorption by aerosol is strongly altitude-dependent and increases with increasing altitude because these aerosols strongly absorb the molecular radiation coming from below. This can lead to underestimation of aerosols confined at low levels (Torres *et al.*, 1998). AI shows the presence of aerosols over Africa and the nearby Atlantic Ocean. Over Africa, the largest values of AI are found between 15°N and 30°N, close to some well-known sources of mineral dust, namely the Bodélé depression over Chad, southern Algeria, northern Mali and Mauritania. The mid-level wind that transports dust is mainly easterly (see the 700 hPa wind vectors in Figure 2(b)). In consequence, dust was exported out of Africa over the Atlantic Ocean. It was then embedded in the southwesterly flow associated with the cyclonic circulation centred around 30°W, 45°N. This flow advected the dust towards Portugal. Such dust episodes are rather typical of the meteorological conditions that prevail in August, with a high-pressure system located over northern Africa and a cyclonic circulation to the west. However, the high usually found over Libya (Moulin *et al.*, 1998) was shifted westward over Morocco here.

In the Meso-NH REF simulation, the areas with aerosol burden larger than 0.1 $g\,m^{-2}$ (Figure 2(b)) match those with the largest AI values well. These include the areas close to the West African sources, the dust outflow over the ocean and the return flow between the Azores and Portugal. As dust can be considered as a dynamic tracer, this result suggests that the low-level circulation is well resolved by the Meso-NH model, nudged toward the ECMWF analyses here. In the northeastern corner, i.e. at latitudes higher than 50°N, dust is incorrectly simulated because the lack of vegetation for a particular land-cover type ('no vegetation with rocks' and 'bare soil' including sand beaches) is assumed to be a potential dust-source zone. In the southeastern corner, e.g. over Niger, the simulated dust load appears too low when compared with the AI feature. This underestimation may be due to the lack of east African sources in the simulation domain. For example, Flamant *et al.* (2009) identified dust sensed over Niger in summer 2006 as mobilized from eastern African remote sources (Bodélé and Sudan) three days earlier. Therefore, the evaluation of the model skill in predicting dust in this area would benefit from a simulation with a larger domain. The quantitative transport of dust over Europe is, however, not affected by the mismatch over Niger, as shown below.

The comparison between the OMI AI and the Meso-NH dust burden gives a qualitative assessment of the mobilization and transport of dust from West Africa. The lidar simulator further allows for a quantitative comparison between observation and simulation. From the CALIOP

Copyright © 2011 Royal Meteorological Society

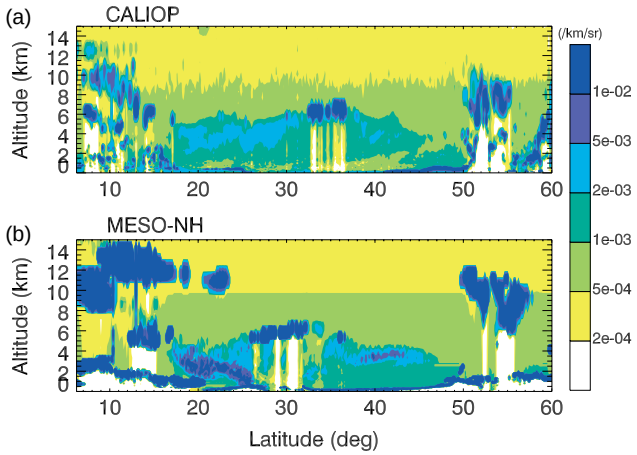

Figure 3. Vertical cross-section of ATB signal at 532 nm ($km^{-1}\,sr^{-1}$) at 0300 UTC on 29 July 2007 along the line shown in Figure 2(b), from (a) CALIOP and (b) Meso-NH. This figure is available in colour online at wileyonlinelibrary.com/journal/qj

observations (Figure 3(a)), the vertical structure of clouds and aerosols can be assessed over a long range, here the west of Africa at 0300 UTC on 29 July (see the CALIPSO track in Figure 2(b)). As checked using a Meteosat Second Generation (MSG) image at 10.8 μm, observed ATB signals larger than $10^{-2}\,km^{-1}\,sr^{-1}$ are due to clouds here: high clouds around 10°N and 50°N, midlevel clouds around 35°N and planetary boundary-layer (PBL) clouds near 25°N and 45°N. Consistent with the OMI retrievals, the dust outflow over the ocean and the return flow between the Azores and Portugal stand around the midlevel clouds, between 2 and 4 km altitude. Dust is characterized by ATB signals around $10^{-3}\,km^{-1}\,sr^{-1}$. Because of the greater distance from African sources, the return flow shows a lower ATB signal than the outflow.

The Meso-NH REF simulation reproduced the features of the vertical structure (Figure 3(b)) that were observed. High clouds associated with tropical deep convection at 10°N and the midlatitude weather system at 50°N were simulated at the right latitude. However, the larger simulated ATB signal suggests too great a detrainmnent of ice, also at too-high altitudes. At 30°N, midlevel clouds were simulated at the right level, but a few degrees too far south and over too large a region. In between these midlevel clouds, the two branches associated with the dust outflow and the return flow spanned the right latitude range. The southern branch associated with the outflow showed a larger ATB signal than observed. At 26°N the simulated dust appeared to be emitted from the surface and did not stand above the oceanic PBL as observed. In contrast, the northern branch associated with the return flow correctly displayed a dust layer floating between 2 and 4 km altitude, with a lower ATB signal than the outflow. The good agreement seen off the northern African coasts was further achieved over Europe as discussed in the next section.

3.2. *Saharan dust reaching France*

Embedded in low-level southwesterlies, the dust layer reached the Iberian Peninsula and western France on 1 August (Figure 4(a)). An easterly branch expanded over the Atlantic Ocean west of 30°W. Over Africa, the AI remained high, illustrating the persistence of the dust

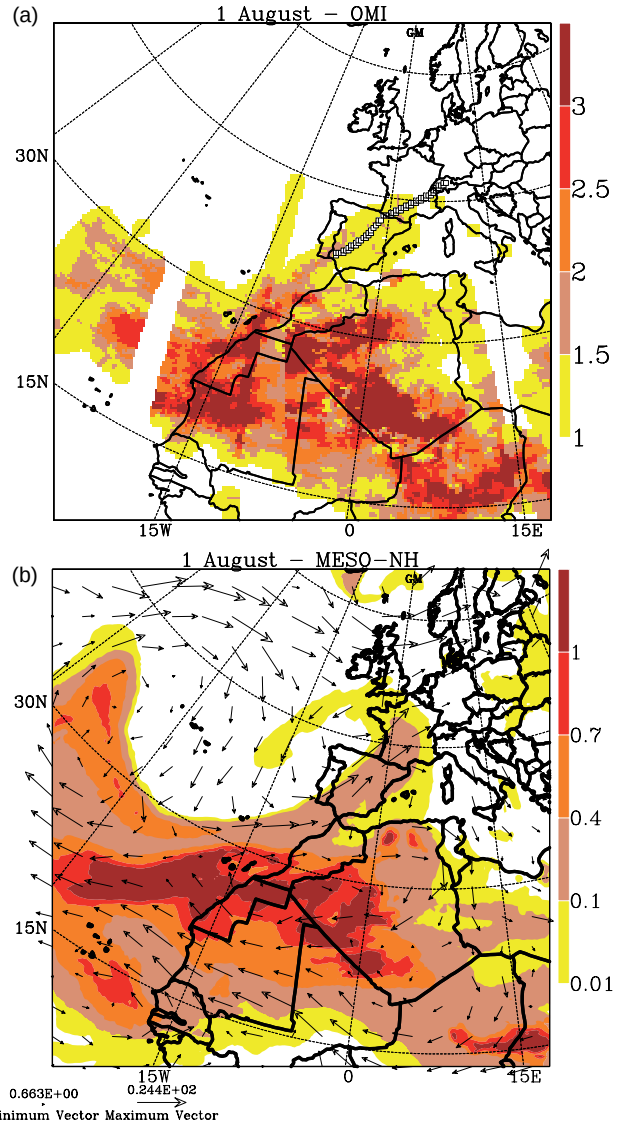

Figure 4. As in Figure 2 but at 1200 UTC on 1 August 2007. The squares in (a) indicate the track of the DLR Falcon. This figure is available in colour online at wileyonlinelibrary.com/journal/qj

emission. Northerlies over the North African coasts turning to easterlies over the Sahara were still prevalent (Figure 4(b)). The simulated dust burden showed several similarities with the retrieved AI, in terms of both structure and amplitude. Again, a smaller dust burden was simulated in the southeastern corner due to the proximity of the domain border. Lower values were also found over Southern Algeria, which can be explained by the lack of dust transported over a range longer than the simulation domain. On the other hand, the western extent of dust over the Atlantic Ocean looked correct, as did the dust load that spread up to western France. This spread in dust over France was confirmed by the comparison with the DLR observations as discussed in the following.

The DLR Falcon flew over the southwesterly flow between Faro, Portugal, and Oberpfaffenhofen, Germany, as this area was targeted as a sensitive region for quantitative precipitation forecast over the COPS region. The vertical cross-section of the ATB signal at 1064 nm is shown in Figure 5. Consistent with the OMI retrievals, the dust layer extended up to 45°N. This layer was relatively moist, with a water-vapour mixing ratio larger than 2 $g\,kg^{-1}$, compared with the

Copyright © 2011 Royal Meteorological Society

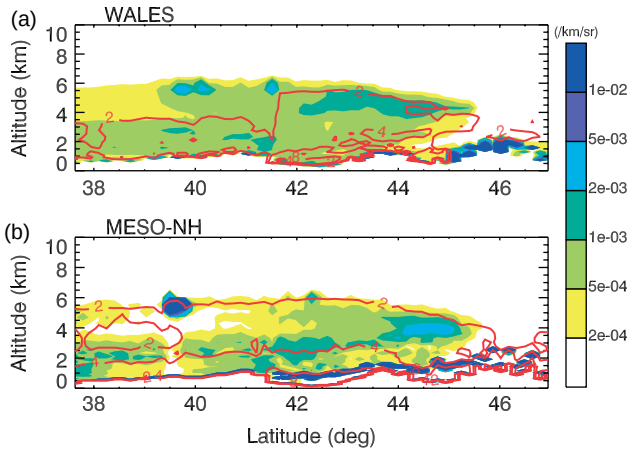

Figure 5. Vertical cross-section of ATB signal at 1064 nm (shading, $km^{-1}\,sr^{-1}$) and water-vapour mixing ratio (contours at 2, 4, 8 $g\,kg^{-1}$) on 1 August 2007 along the line shown in Figure 4(b), from (a) WALES between 0900 and 1100 UTC and (b) Meso-NH at 1200 UTC. This figure is available in colour online at wileyonlinelibrary.com/journal/qj

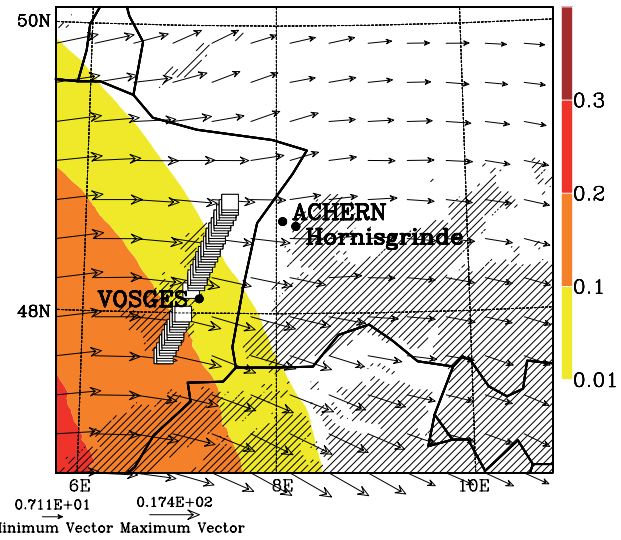

Figure 6. Total aerosol burden ($g\,m^{-2}$) and 4 km wind vectors at 1600 UTC on 1 August 2007. The squares indicate the track of the SAFIRE Falcon. Hatched areas indicate topography above 500 m. The domain is 400 km long. This figure is available in colour online at wileyonlinelibrary.com/journal/qj

dry conditions prevailing further north. Isolated maxima of backscattered signal at 6 km altitude also indicated the presence of clouds on top of the dust layer. Below the leading edge of the dust layer, a tongue of dry air could be seen at 2 km altitude. The origin of this layer is identified in the following as subsiding air from the midtroposphere.

The Meso-NH REF simulation presented a vertical structure with a dust and moist air layer extending from the surface up to about 6 km (Figure 5(b)). The moist air mass was topped by clouds with ATB signal larger than $2 \times 10^{-3}\,km^{-1}\,sr^{-1}$. South of 42°N, the simulation missed the water-vapour drop between 4 and 6 km altitude. The simulated dust was located around 3 km altitude along most of the cross-section. This is at about the right position in the southern part, but at too low an altitude at 43°N across the Pyrenees mountains and with too high an ATB signal at 44°N.

3.3. *Saharan dust over the Vosges*

In the afternoon, the Saharan dust layer reached north-eastern France within a westerly flow at 4 km altitude (Figure 6). At 1600 UTC on 1 August the simulated dust burden was organized as a smooth front with values around 0.1 $g\,m^{-2}$. Around that time, the dust layer was sampled by the LEANDRE 2 lidar operating over the Vosges mountains. The observed and simulated vertical cross-sections of the 730 nm ATB signal and water-vapour mixing ratio are shown in Figure 7. Two distinct layers of particles were observed, while a single layer was simulated.

Between 3 and 5 km altitude, the dust layer was associated with values of water-vapour mixing ratio larger than 2 $g\,kg^{-1}$. It could be further divided into two sub-layers. The upper layer extended further to the north than the lower one and showed higher ATB values. In the simulation, the leading edge of this layer was properly located. The water-vapour mixing ratio was also in good agreement with the observations. However, the stratification of the ATB signal differed in the southern part by showing a single and rather diffusive layer of dust. This could be attributed to the lower vertical resolution of the model, 600 m here compared with 200 m analyzed for water vapour from the lidar signal.

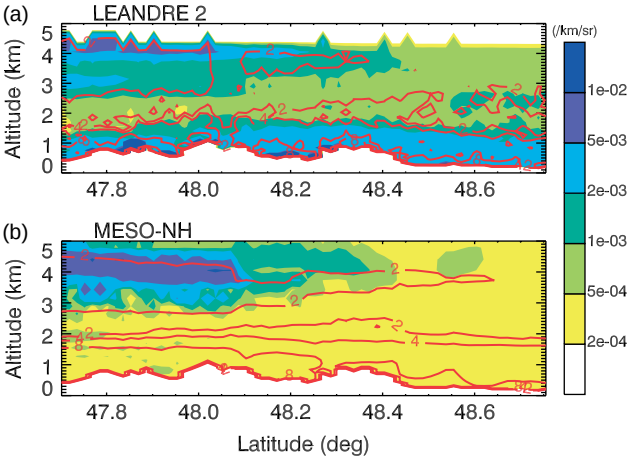

Figure 7. Vertical cross-section of ATB signal at 730 nm (shading, $km^{-1}\,sr^{-1}$) and water-vapour mixing ratio (contours at 2, 4, 8 $g\,kg^{-1}$) at 1600 UTC on 1 August 2007 along the line shown in Figure 6(c), from (a) LEANDRE 2 and (b) Meso-NH. This figure is available in colour online at wileyonlinelibrary.com/journal/qj

In the first km agl, the observed PBL is filled with background aerosols. As only dust aerosol was simulated, the scattered signal close to the ground was missed by the model. On the other hand, the PBL top corresponded in the observation with the water-vapour mixing ratio value of 4 $g\,kg^{-1}$ at 2 km altitude. The correct position of the simulated 4 $g\,kg^{-1}$ isoline suggests the right vertical depth of the PBL in the model. Note also the moist bias in the first hundred metres agl. This bias is currently under investigation, as it was noticed in other COPS case studies (Richard *et al.*, 2011).

3.4. *Arrival of dust over Achern*

At 1700 UTC on 1 August, the dust layer arrived over the COPS area as observed by the BASIL Raman lidar operating at Achern, Germany (Figure 8(a)). The PBL, with a thickness of about 1.5 km, was characterized by a mixing ratio higher

Copyright © 2011 Royal Meteorological Society

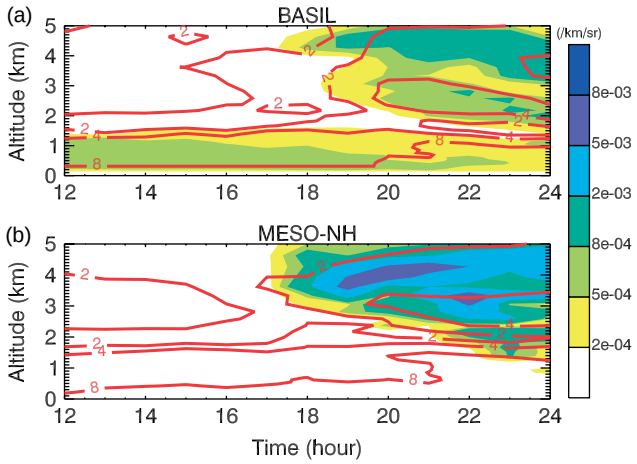

Figure 8. Time series of β_{par} at 1064 nm (shading, $km^{-1}\ sr^{-1}$) and water-vapour mixing ratio (contours at 2, 4, 8 $g\,kg^{-1}$) over Achern from 1200 UTC on 1 August to 0000 UTC on 2 August 2007, for (a) BASIL and (b) Meso-NH. This figure is available in colour online at wileyonlinelibrary.com/journal/qj

than 4 $g\,kg^{-1}$ and a particle backscatter coefficient β_{par} larger than 2×10^{-4}. Due to its location in the PBL, this coefficient could be identified as representative of background aerosol. At 2000 UTC, the depth of the layer with mixing ratio larger than 8 $g\,kg^{-1}$ increased while β_{par} decreased, suggesting a change in air mass. A first change in air mass occurred just above 1.5 km at 1600 UTC with the arrival of dry air with mixing ratio values smaller than 2 $g\,kg^{-1}$. At 1800 UTC this air mass was replaced by a dusty one above 2 km while the dry layer remained beneath. Consistent with the LEANDRE 2 observation, the dust layer could be divided into two sub-layers. The one located between 3 and 5 km gave more backscattering than the layer below, the latter being moister with a water-vapour mixing ratio larger than 4 $g\,kg^{-1}$.

The Meso-NH REF simulation shows good agreement with the observations in capturing the height and arrival time of the dust layer (Figure 8(b)). However, the dust layer lacks the fine-scale structure sensed by BASIL, showing a dust contribution to the lidar signal spanning too thick a layer. Note also the absence of lidar signal in the first km due to the lack of background aerosols in the simulation. On the other hand, the simulated water-vapour mixing ratio is in agreement with the BASIL measurements. For example, the increase in water vapour at 2000 UTC is simulated in the first km, as is the arrival of the dry layer first in the free troposphere then just above the PBL. This is also true for the pocket of enhanced water-vapour values over 4 $g\,kg^{-1}$ found around 3 km. These results give us confidence in the simulated transport of air masses.

In order to check the origin of air masses, backward trajectories (Gheusi and Stein, 2002) were computed. Parcels in the same vertical column over Achern were taken at altitudes of 1, 2, 3 and 4 km and their origins six days earlier were determined (Figure 9). Parcels at 4 km altitude show backward trajectories that follow the pathways of the dust burden seen in Figures 2(b) and 4(b). This clearly confirms the origin of dust as northern Africa. Parcels at 3 km altitude can be traced back to the PBL over the Atlantic Ocean. This result agrees well with the spectral analyses of the BASIL observations. Using information provided by the BASIL measurements at three wavelengths, the layer content was identified as a mixture of dust and sea salt. Parcels at 2 km altitude were characterized by clean and relatively dry air.

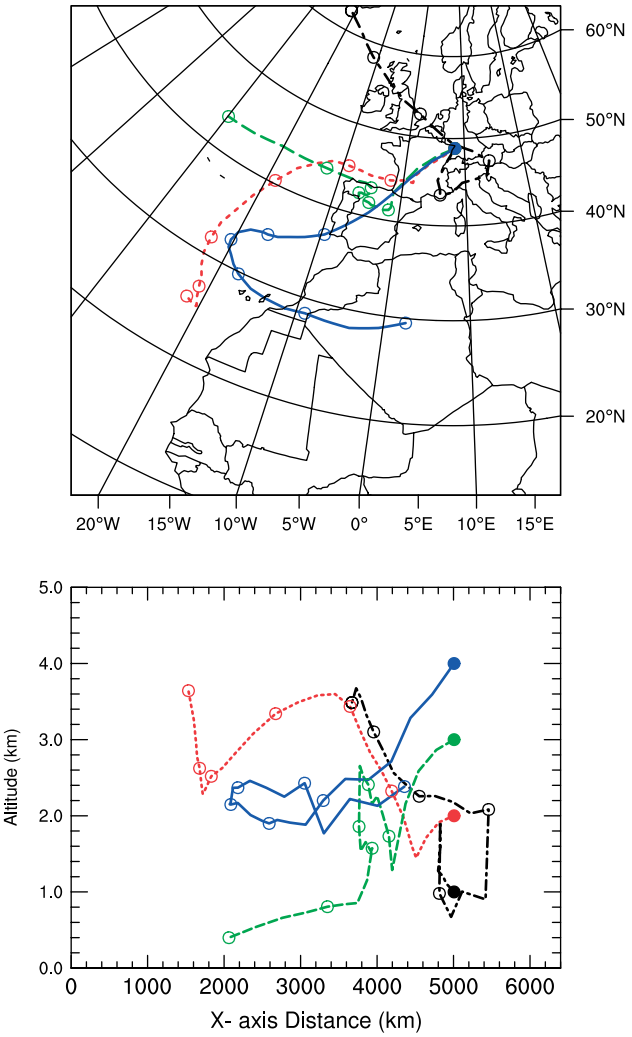

Figure 9. Backward trajectories from 0000 UTC on 27 July 2007 to 0000 UTC on 2 August 2007. Panel (b) represents a projection of the trajectories along the *x*-axis of the simulation domain. Circles on the backward trajectories are spaced at 24 h intervals; the filled circles show the starting points. This figure is available in colour online at wileyonlinelibrary.com/journal/qj

On 28 July, the parcels subsided from 4 to 1.5 km over the Atlantic Ocean. Their midtropospheric origin explains the low water-vapour content, around 2 $g\,kg^{-1}$, well. Finally, parcels at 1 km altitude came from the Rhone valley two days earlier. In the valley, there are many cities, industrial plants and motorways. These anthropogenic sources explain the large background aerosol content measured by BASIL. This signal was missed by Meso-NH as no urban aerosol was simulated.

3.5. *Observation of dust over Hornisgrinde*

As further evidence of dust over the COPS area, the UHOH DIAL lidar operating at Hornisgrinde, Germany also showed the arrival of dust at 1700 UTC on 1 August (Figure 10(a)). As for the previous lidar observations, the dust air mass between 2 and 5 km was made up of two sub-layers, the highest being dustier and drier. In contrast to the BASIL observation, less background aerosol was sensed by the UHOH lidar at lower altitudes as it was operated at 1161 m on top of the northern Black Forest. As for the previous comparison, the Meso-NH simulation (Figure 10(b)) shows

Copyright © 2011 Royal Meteorological Society

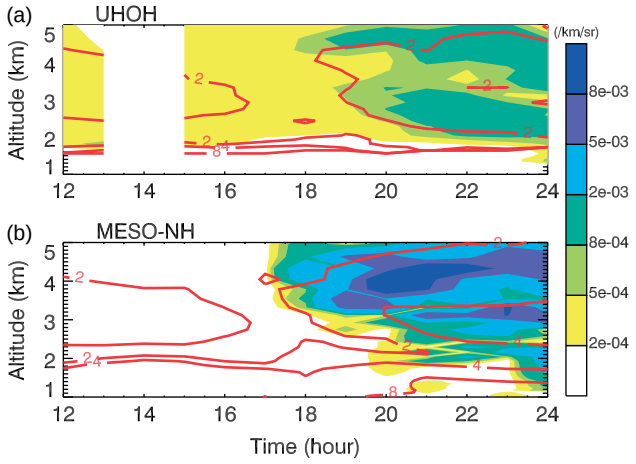

Figure 10. Time series of β_{par} at 820 nm (shading, $km^{-1}\ sr^{-1}$) and water-vapour mixing ratio (contours at 2, 4, 8 $g\,kg^{-1}$) over Hornisgrinde from 1200 UTC on 1 August 2007 to 0000 UTC on 2 August 2007, for (a) UHOH and (b) Meso-NH. This figure is available in colour online at wileyonlinelibrary.com/journal/qj

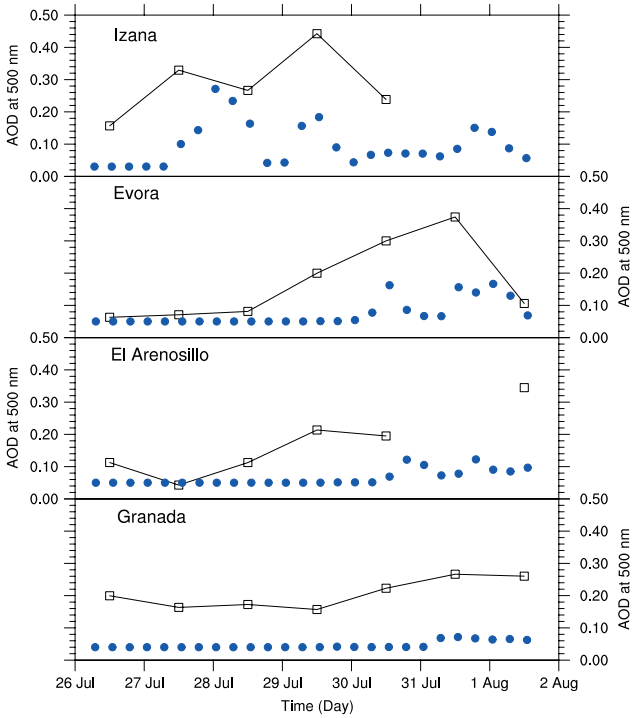

Figure 11. Time evolution of AOD at 500 nm from AERONET (line) and Meso-NH (points) for Izana, Evora, El Arenosillo and Granada from 26 July–2 August 2007. This figure is available in colour online at wileyonlinelibrary.com/journal/qj

good agreement in the timing of the dust arrival, while the fine-scale layering is missed by the model. Above 2 km, the water-vapour content shows a similar pattern to the one probed by the nearby BASIL lidar. The Meso-NH REF simulation therefore reproduced the water-vapour features over Hornisgrinde as well as over Achern.

4. Quantitative evaluation of dust

A quantitative evaluation of dust content from the Meso-NH REF simulation was made by comparison with retrievals of aerosol optical thickness (AOD) at AErosol RObotic NETwork (AERONET) stations in the dust pathway, i.e. Izana in the Canaries and stations in the southern Iberian Peninsula (Evora, El Arenosillo and Granada). Their locations are indicated in Figure 1. The AOD at 500 nm is shown in Figure 11. The highest level data were used, i.e. Level 2 (cloud-screened and quality-assured) at Granada and Evora and Level 1.5 (cloud-screened) at Izana and El Aranesillo. At Izana, AOD was observed with values ranging between 0.1 and 0.4. The signal magnitude of 0.3 can be attributed to the dust outbreak. This value matches well the AOD increase observed at Evora on 31 July and at El Aranesillo on 1 August. Further to the east (Granada), the variation in AOD was very small, less than 0.1. These short-distance changes in AOD are consistent with the narrow feature of large OMI AI retrievals seen over the Iberian Peninsula (Figure 4(a)).

In the simulation, AOD results in a variable dusty part in addition to the climatological contribution (urban, sea and land aerosols). At Izana, two peaks of 0.28 and 0.19 were simulated on 27 and 29 July, which match the observed peaks within a few hours (there was no observation during night-time). At Evora, the simulated change in AOD was lower than observed, 0.11 against 0.31. At El Arenosillo and Granada, the dust outbreak affected the AOD only marginally, with an increase of less than 0.1. (Note that the background AOD value is correct at El Arenosillo and underestimated by 0.1 at Granada.) This dust outbreak, small and limited in space, was simulated with good agreement with AERONET measurements.

The quantitative evaluation was pursued with scatter plots of observation and simulation for the lidar signal and the water-vapour mixing ratio. In Figure 12, the comparison is made between ground level and 5 km altitude using observed and simulated profiles previously shown in Figures 5, 7, 8 and 10. A large underestimation of the simulated lidar signal occurs below 2 km altitude, as shown with plus signs. This severe discrepancy is due to the PBL background aerosols, which were not taken into account in the simulation of the lidar signal. Above this altitude, observed and simulated lidar signals are organized along the 1:1 line but with large deviation that can reach a factor of 10. This highlights the differences in the position and intensity of the lidar signals shown in the previous figures. The discrepancy is also less severe for LEANDRE 2 and WALES than for BASIL and UHOH, the latter probing more aged dust aerosols than the former. This enhanced overestimation with time might therefore be partly explained by the absence of coating considered in the simulation, as the coating of dust with soot increases the absorption coefficient with respect to dust alone (Müller *et al.*, 2009), which in turn reduces the backscattered signal. The observed time-dependent overestimation might also be due to the evolution of the microphysical aerosol properties, as well as the way the size distribution is described in the model.

The scatter plots of the water-vapour mixing ratio show good correspondence between observation and simulation, with correlation-coefficient values ranging between 0.75 and 0.89. However, as shown by the linear regression lines, Meso-NH is moister than the lidar retrievals. The biases range between 0.62 and 1.32 $g\,kg^{-1}$. They are larger for UHOH and WALES than for BASIL and LEANDRE 2. This is consistent with the COPS water-vapour intercomparison study showing a slightly dry bias for the former lidar systems

Copyright © 2011 Royal Meteorological Society

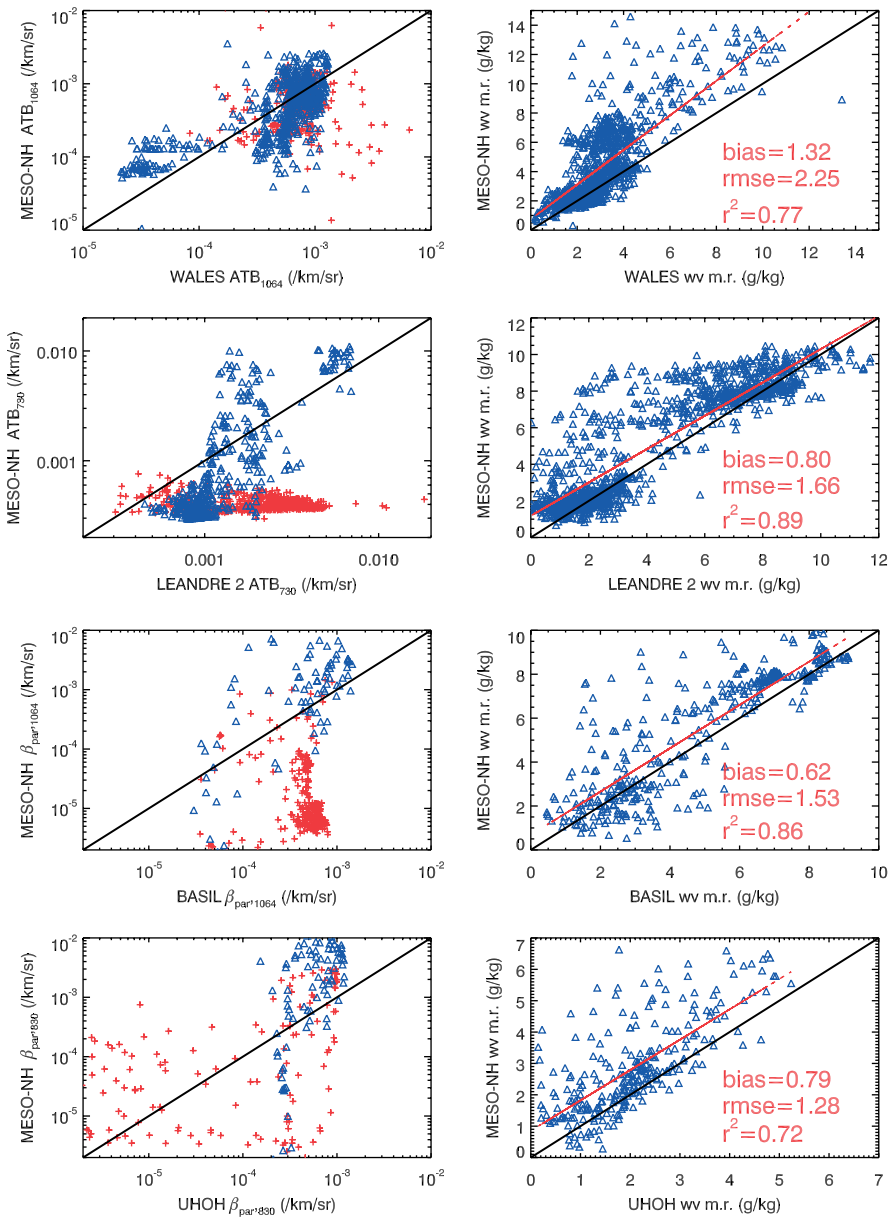

Figure 12. Scatter plots of simulation versus observation for (left) backscatter signal (either ATB or β_{par}) and (right) water-vapour mixing ratio for lidar observation and Meso-NH between ground level and 5 km altitude. The thick black line represents the 1:1 line. Backscatter signals measured below 2 km altitude are plotted with plus signs. The linear regression line, bias, RMSE and correlation coefficient are given for water vapour. This figure is available in colour online at wileyonlinelibrary.com/journal/qj

compared with the latter (Bhawar *et al.*, 2011). The root-mean-square error (RMSE) is between 1.43 and 2.25 g kg^{-1}. The largest value is found for WALES because of the larger variability of water vapour under scrutiny during the long-range flight operated by the DLR Falcon.

5. Impact on precipitation forecasts

The sensitivity of the precipitation forecast to the radiative impact of the dust layer was investigated using three simulations described in section 2.2: DUST using the dust prognostic scheme, CLIM using a climatology of dust as applied in some operational numerical weather prediction models and NODUST, which does not consider any dust effect. Only the radiative effect of dust was considered here. No interaction between dust aerosols and clouds was taken into account. Simulations were run over five days to allow the dust to have a sufficient radiative impact on the thermodynamic structure of the atmosphere.

The differences in temperature between DUST and the other two experiments were limited to small values, around 2 K, and below the 6 km altitude as imposed in the simulation set-up. These small changes appeared to be always positive when compared with radiosonde data at 1200 UTC on 1 August. Among the stations examined over Spain and France, the example with the largest change was Zaragoza, Spain (41.66°N, 1.01°W; Figure 13). From ground level to 750 hPa, i.e. within the dust layer, the temperature was enhanced by a few K in DUST compared with NODUST and CLIM. The largest increase, 3.4 K, occurred at 910 hPa (830 m altitude). In particular, this increase made the DUST temperature profile closer to the observed one.

The net impact of dust alone was examined by showing the differences in temperature together with the dust concentration over the simulation domain (Figure 14(a)).

Copyright © 2011 Royal Meteorological Society

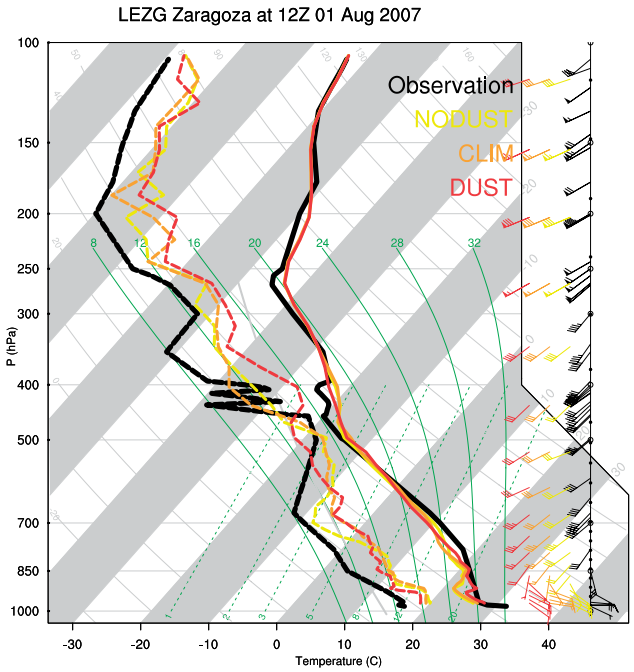

Figure 13. Skew-*T* diagram over Zaragoza, Spain at 1200 UTC on 1 August 2007 for observation (thick line) and simulations (thin lines). This figure is available in colour online at wileyonlinelibrary.com/journal/qj

This is shown at 2 km altitude where the temperature differences span a large area. As expected, the difference between DUST and NODUST experiments showed an increase in temperature in dust areas (including Zaragoza). The increase was rather uniform where dust occurred. The largest increase, about 2 K at most, occurred in the northwestern part of the domain where the dust concentration was the highest. Otherwise, the increase at 2 km altitude was moderate. Elsewhere, i.e. in areas without any dust, the difference in temperature appeared as a random perturbation of ±0.5 K. The radiative perturbation in dust generated small differences in temperature, which in turn changed results of the physical parametrizations such as the convection scheme or the subgrid cloud scheme.

A vertical cross-section of differences in potential temperature between 20°N and 50°N provided details of the net impact of dust on the vertical structure (Figure 14(c)). Overall, the potential temperature increased in the presence of dust. South of 25°N, heating of about 1 K occurred around 5 km altitude in a cloud-free region. Due to attenuation of the incoming solar radiation by dust, the potential temperature in the layers below the dust decreased. North of 30°N, the direct radiative impact of dust during its long-range transport led to an increase in potential temperature larger than 0.5 K. North of 48°N, the potential temperature increased at 2 km and decreased at 5 km. As this area was free of dust, this clearly indicates that dust generates potential temperature perturbations downstream, leading to a decrease in the static stability for the DUST experiment.

As most of the numerical weather prediction models use a dust climatology in order to take its radiative effect into account, the difference between DUST and CLIM experiments allowed us to test the impact of a realistic dust field compared with a climatological one. The difference in potential temperature at 2 km altitude between DUST and CLIM experiments is shown in Figure 14(b). For this summer period, the climatological dust was mainly found over North Africa. In consequence, a decrease in potential temperature between the DUST and CLIM experiments was identified at the southeastern part of the domain due to a larger optical thickness for CLIM there. In contrast, the potential temperature difference over the eastern Atlantic Ocean was similar between DUST and NODUST and DUST and CLIM. In the northeastern part of the domain, the difference was also randomly perturbed by ±0.5 K.

The same location in the vertical cross-section was used to examine the impact on the vertical structure of potential temperature (Figure 14(d)). South of 25°N, as for the difference between DUST and NODUST, the potential temperature increased by 1 K around 5 km altitude and decreased below. This can be explained by the dust radiative effect only. However, the magnitude of the change in potential temperature differs there, as it does northward, suggesting some indirect effects (for example, the triggering of a threshold-based parametrization like the convection scheme). North of 48°N the difference between DUST and CLIM is remarkably similar to the one between DUST and NODUST. As a result, the static stability decreases for the DUST experiment.

The potential temperature increase leads to a modification of the convective available potential energy (CAPE), mostly along the Greenwich Meridian (Figure 15). CAPE is defined as the vertical integral of the lifted-parcel buoyancy from departure level (DPL) to the level of neutral buoyancy. It is based on the pseudo-adiabatic ascent of an air parcel, the DPL of which is from a low level. Here we use the CAPE from the DPL that gives the maximum CAPE value. All the experiments show a maximum of CAPE larger than 2500 J kg^{-1} in southwestern France. At 45°N along the line of the vertical cross-section shown in Figure 14(a) and (b), DUST shows higher CAPE values than NODUST and CLIM. On the other hand, CAPE is larger in NODUST and CLIM than in DUST along the southern French Atlantic coast where the line of thunderstorms triggered, as observed in MSG images.

These small changes in static stability have an impact on the resulting rain shown by 6 h accumulated precipitation valid at 0000 UTC on 2 August 2007 (Figure 16). This 6 h period corresponds to the rain event in which thunderstorms were fully developed over France. Measurements from rain gauges projected on to the 2 km Meso-NH grid show two areas of precipitation larger than 7.5 mm in 6 h, over Limousin (2°E, 46°N) and Burgundy (4°E, 47°N), while the rest of the domain is almost free of precipitation.

In the three experiments, rain was organized along a line with a northeastern orientation. As in the observation, the rainfall line covers Limousin and Burgundy, but spans a larger area. All the experiments overestimated the rain fields in the southwestern tip. They differed in the location of the peak in the northeast. DUST gave rain over Burgundy correctly while the other two experiments predicted additional rain further northeast. A large rain cluster was incorrectly predicted over southwestern France. Again DUST appeared to perform rain prediction better than the other two by showing less precipitation. In consequence, correlation-coefficient values were larger for DUST (0.39) than for NODUST (0.28) and CLIM (0.35).

The ability of the simulations to forecast the rain event at the right place was quantified with the Equitable Threat Score (ETS). ETS measures the correspondence between

Copyright © 2011 Royal Meteorological Society

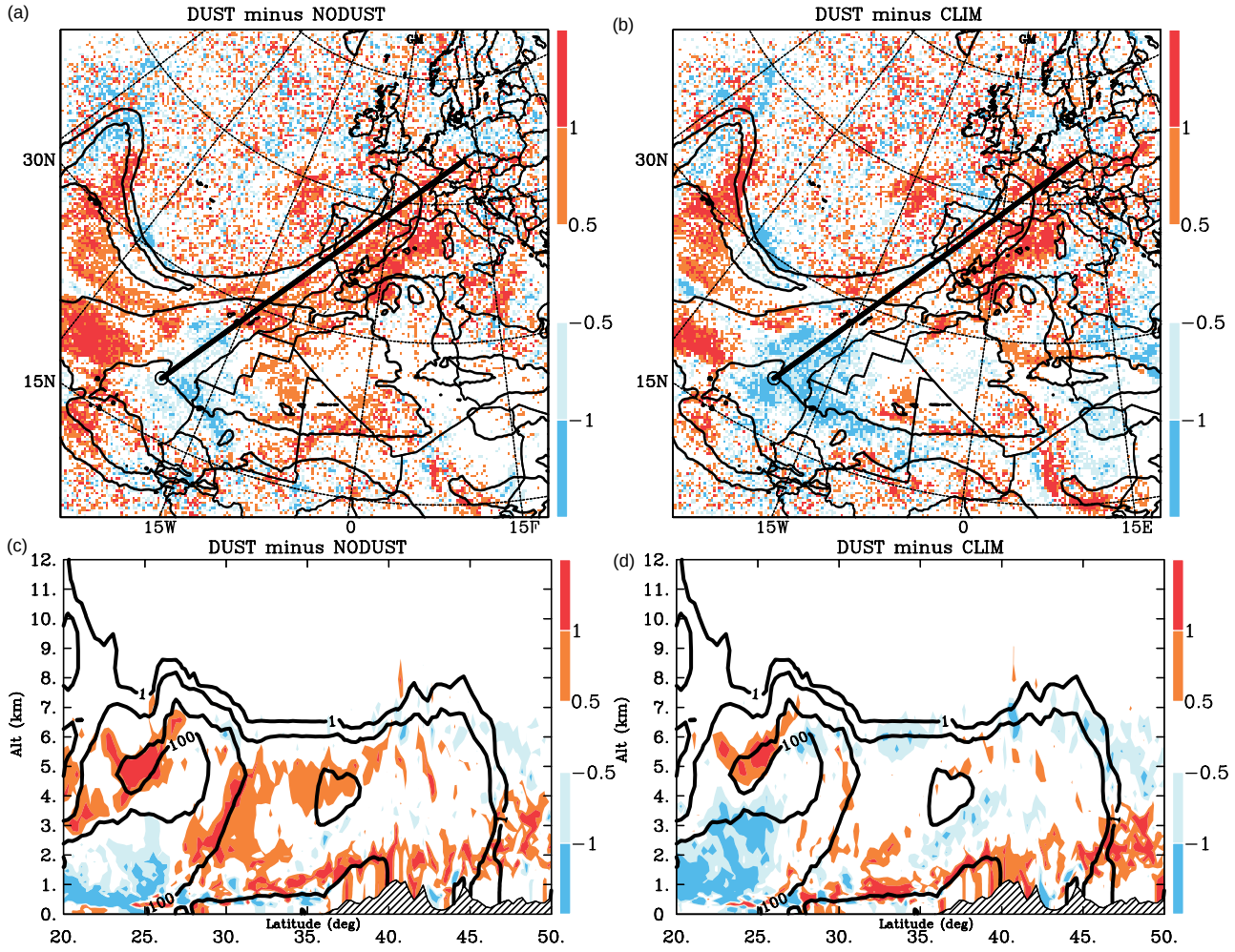

Figure 14. Difference in potential temperature between (a, c) DUST and NODUST and (b, d) DUST and CLIM simulations at 1200 UTC on 1 August 2007. Panels (a) and (b) show the difference at 2 km altitude; the black lines indicate the aerosol burden from DUST (contours at 0.1, 0.5 g m^{-2}). Panels (c) and (d) give the vertical cross-section along the lines shown in (a) and (b); the black lines indicate the dust concentrations from DUST (contours at 1, 10, 100 μg m^{-3}). This figure is available in colour online at wileyonlinelibrary.com/journal/qj

simulated and observed occurrences of events at grid points. It was calculated for the 6 h accumulated rain at 0000 UTC on 2 August over the inner domain (Figure 17(a)). From the 1 mm category and for each simulation, the ETS decreased as the threshold increased. Higher ETS were found for DUST whatever the rain category. This result shows that a better rain forecast was provided, for this particular event, by the simulation using a dust prognostic scheme.

The evaluation of the cloud cover was also examined through comparisons with MSG observations. We used the brightness temperatures (BT) at 10.8 μm, as they are mainly affected by cloud-top heights. Synthetic BTs from simulations were computed using the Radiative Transfer for Tiros Operational Vertical Sounder (RTTOV) code version 8.7 (Saunders *et al.*, 2005). Figure 17(b) shows ETS calculated for BT less than 230 K every hour from 1900 UTC on 1 August to 0000 UTC on 2 August. The 230 K threshold is commonly used to detect deep convective clouds (Söhne *et al.*, 2008). An increase in ETS was observed as the line of thunderstorms developed with time. This shows the ETS sensitivity to the correct prediction of deep convective clouds. In contrast with ETS results for rain, no simulation performed significantly better than the others in forecasting BT less than 230 K. The simulated low BTs spread over a much larger area than the observed BTs (not shown).

6. Conclusions

A Saharan dust event affected the Rhine valley on 1 August 2007 during the COPS experiment prior to a convective event. This case was investigated using lidar observations from space, aircraft and ground and a regional model. The consistency between the different sets of information allowed the sources of dust to be identified. Both observations and simulation supported the fact that dust at 4 km altitude originated from the Sahara six days earlier. In addition, dry air was observed at 2 km altitude by the different water-vapour lidar systems operating over France and Germany. The agreement with the simulation allowed the dry air to be traced back as subsiding five days earlier from the midtroposphere over the Atlantic Ocean. This consistency between observations and simulation gives us further confidence in the identification of the aerosol observed at 3 km altitude over Achern as a mixture of dust and sea salt.

The direct comparison between observed and simulated backscattered signals shows the good performance of the model in terms of characterization and transport of dust.

Copyright © 2011 Royal Meteorological Society

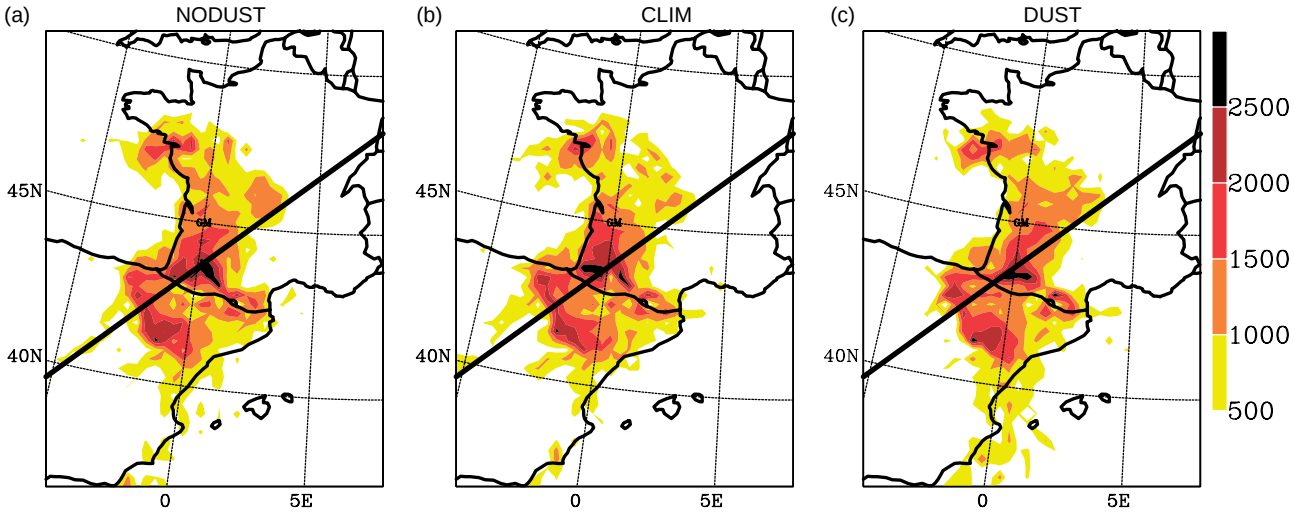

Figure 15. CAPE (J kg^{-1}) at 1200 UTC on 1 August 2007 for (a) NODUST, (b) CLIM and (c) DUST experiments. The line indicates the position of the vertical cross-section shown in Figure 14(a) and (b). This figure is available in colour online at wileyonlinelibrary.com/journal/qj

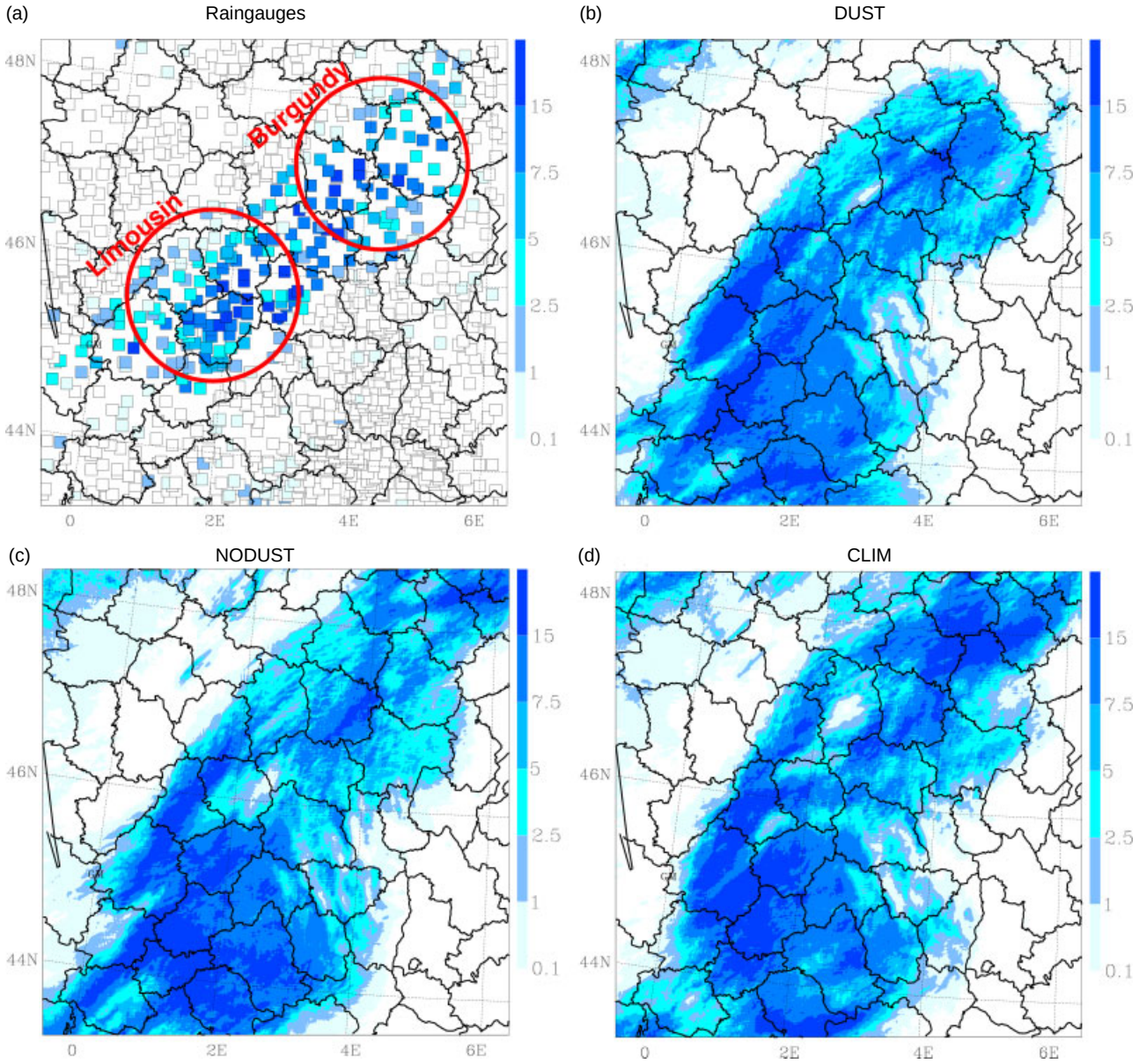

Figure 16. Six-hour accumulated precipitation (mm) valid at 0000 UTC on 2 August 2007 from (a) rain gauges (over France only), (b) DUST, (c) NODUST and (d) CLIM experiments. The domain is 576 km long. Longitude and latitude lines are plotted every 2°. This figure is available in colour online at wileyonlinelibrary.com/journal/qj

Copyright © 2011 Royal Meteorological Society

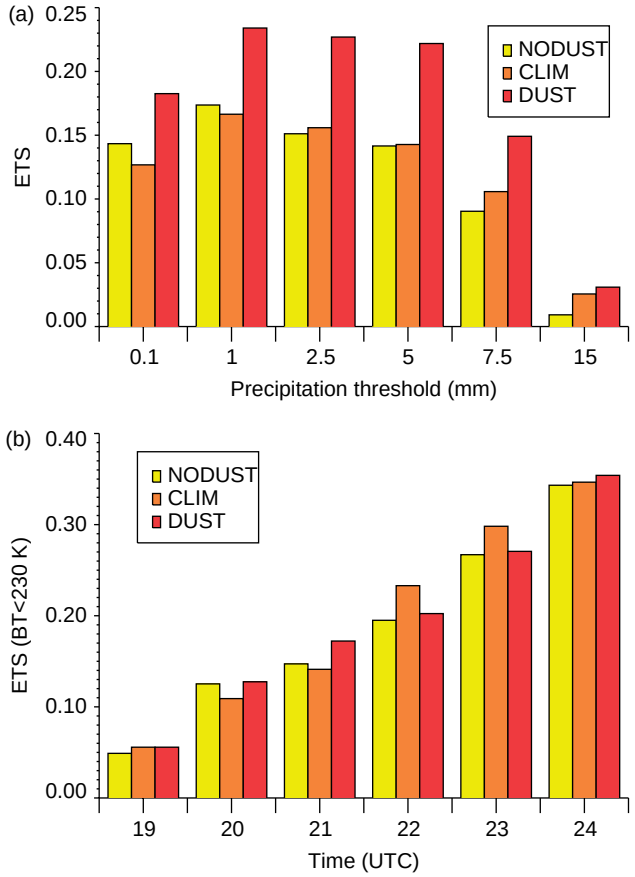

Figure 17. Equitable Threat Score (ETS) for (a) 6 h accumulated precipitation (mm) at 0000 UTC on 2 August 2007 and (b) 10.8 μm BT less than 230 K at 1900, 2000, 2100, 2200 and 2300 UTC on 1 August 2007 and 0000 UTC on 2 August 2007. This figure is available in colour online at wileyonlinelibrary.com/journal/qj

The lidar simulator developed here is shown to be a powerful tool for evaluation. This simulator will be used for many other applications. Its use is foreseen for the evaluation of case studies such as those observed during the African Monsoon Multidisciplinary Analysis (AMMA) campaign (Flamant *et al.*, 2007) and those from which an estimate of dust emission was made (Bou Karam *et al.*, 2009). The simulator still needs further development to take account of the non-spherical shape of cirrus crystals, which will be modelled by a sophisticated microphysics cloud scheme.

The radiative impact of dust on precipitation forecasts was also investigated. Three simulations, with or without the dust prognostic scheme or using a dust climatology, were run forward for five days. The radiative effect of dust generated some perturbations in temperature. The latter resulted in a change in static stability. Here, the enhancement of dust over France led to a decrease in static stability along the thunderstorm path. In consequence, precipitation showed better agreement with rain gauges as assessed with the skill score. This suggests that skill in rain forecasts could be increased in the five-day range by using a prognostic scheme during dust episodes reaching Europe.

Finally, only the radiative impact of dust was taken into consideration in this study although some evidence exists that mineral dust alters cloud microphysics and precipitation. For example, Min *et al.* (2009) found that the microphysical effects of the dust aerosols could shift the precipitation size spectrum from heavy precipitation to light precipitation and ultimately suppress precipitation. In the future, we foresee the investigation of these effects on precipitation forecasts. The lidar simulator is a precious tool with which to constrain the initialization of the dust load along with the other instrument emulators for examining the cloud and precipitation fields. Also, the aerosol analysis carried out by general circulation models such as ECMWF (Morcrette *et al.*, 2009) will provide the initial and lateral conditions needed by the regional models. This research effort will be conducted within the preparation of the future Hydrological Cycle in the Mediterranean eXperiment (HyMeX) field campaign (http://www.cnrm.meteo.fr/hymex/).

Acknowledgements

The support of WWRP in the scientific planning of COPS and the excellent collaboration with the D-PHASE modelling community were greatly appreciated. COPS is a component of Priority Programme 1167 funded by the German Research Foundation. We thank DWD for providing COSMO-EU forecasts for model evaluation. The ARM programme, funded by the US Department of Energy's Environmental Sciences Division, made the unique AMF available to COPS. COPS is further supported by CNRS/INSU (Institut des Sciences de l'Univers), CNES (Centre National de la Recherche Spatiale), ANR (Agence Nationale pour la Recherche) and Météo-France, as well as by the Austrian Science Foundation (FWF) and the University of Vienna. Detailed information on scientific coordination is available on the COPS International web site (http://www.uni-hohenheim.de/spp-iop/). We thank SAFIRE (Service des Avions Français Instrumentés pour la Recherche en Environnement), the Institut Géographique National (IGN) and the Technical division of INSU (DT/INSU) for preparing and delivering the research aircraft (Falcon 20/F-GBTM) and the airborne instruments in a timely manner for COPS. We are grateful to D. Bruneau and P. Genau (LATMOS), F. Blouzon, A. Abchiche and N. Amarouche (DT/INSU) for re-fitting and operating the LEANDRE 2 system in the F/F20. Special thanks to A. Gribkoff, R. Cailloux and M. Laurens (SAFIRE) for operating the dropsonde system. The CALIPSO data were obtained from the ICARE Data and Services Centre. Computer resources were allocated by IDRIS. Rain-gauge data were provided by Météo-France. We thank P. Goloub, A. M. Silva, V. E. Cachorro Revilla and L. Alados Arboledas for maintening the AERONET sites cited in this study and Juan Cuesta for useful discussions concerning aspects of this work.

References

Alfaro SC, Gomes L. 2001. Modeling mineral aerosol production by wind erosion: Emission intensities and aerosol size distributions in source areas. *J. Geophys. Res.* **106**: 24671–24687.

Alpert P, Kishcha P, Shtivelman A, Krichak SO, Joseph JH. 2004. Vertical distribution of Saharan dust based on 2.5-year model predictions. *Atmos. Res.* **70**: 109–130.

Ansmann A, Bosenberg J, Chaikovsky A, Comeron A, Eckhardt S, Eixmann R, Freudenthaler V, Ginoux P, Komguem L, Linne H, Marquez MAL, Matthias V, Mattis I, Mitev V, Muller D, Music S, Nickovic S, Pelon J, Sauvage L, Sobolewsky P, Srivastava MK, Stohl A, Torres O, Vaughan G, Wandinger U, Wiegner M. 2003. Long-range transport of Saharan dust to northern Europe: The 11–16 October 2001 outbreak observed with EARLINET. *J. Geophys. Res.* **108**: DOI:10.1029/2003JD003757

Copyright © 2011 Royal Meteorological Society

Barkan J, Alpert P, Kutiel H, Kishcha P. 2005. Synoptics of dust transportation days from Africa toward Italy and central Europe. *J. Geophys. Res.* **110**: D07208. DOI:10.1029/2004JD005222

Bechtold P, Bazile E, Guichard F, Mascart P, Richard E. 2001. A mass flux convection scheme for regional and global models. *Q. J. R. Meteorol. Soc.* **127**: 869–886.

Behrendt A, Wulfmeyer V, Riede A, Wagner G, Pal S, Bauer H, Radlach M, Späth F. 2009. 3-dimensional observations of atmospheric humidity with a scanning differential absorption lidar. In *Proceedings of SPIE – The International Society for Optical Engineering, Volume 7475, Article number 74750L*. SPIE: Bellingham. DOI: 10.1117/12.835143

Bhawar R, Di Girolamo P, Summa D, Flamant C, Althausen D, Behrendt A, Kiemle C, Bosser P, Cacciani M, Champollion C, Di Iorio T, Engelmann R, Herold C, Pal S, Wirth M, Wulfmeyer V. 2011. The water vapour intercomparison effort in the framework of the Convective and Orographically-induced Precipitation Study: airborne-to-ground-based and airborne-to-airborne lidar systems. *Q. J. R. Meteorol. Soc.* **137**(S1): 325–348, DOI: 10.1002/qj.697

Bohren CF, Huffman DR. 1985. *Absorption and scattering of light by small particles*. John Wiley and Sons.

Bou Karam D, Flamant C, Tulet P, Chaboureau JP, Dabas A, Todd MC. 2009. Estimate of Sahelian dust emissions in the inter-tropical discontinuity region of the West African Monsoon. *J. Geophys. Res.* **114**: D13106. DOI:10.1029/2008JD011444

Brenot H, Ducrocq V, Walpersdorf A, Champollion C, Caumont O. 2006. GPS zenith delay sensitivity evaluated from high-resolution numerical weather prediction simulations of the 8–9th September 2002 flash flood over southeastern France. *J. Geophys. Res.* **111**: DOI:10.1029/2004JD005726

Caumont O, Ducrocq V, Delrieu G, Gosset M, Pinty JP, Parent du Châtelet J, Andrieu H, Lemaître Y, Scialom G. 2006. A radar simulator for high-resolution nonhydrostatic models. *J. Atmos. Oceanic Technol.* **23**: 1049–1067.

Chaboureau JP, Bechtold P. 2002. A simple cloud parameterization derived from cloud resolving model data: diagnostic and prognostic applications. *J. Atmos. Sci.* **59**: 2362–2372.

Chaboureau JP, Bechtold P. 2005. Statistical representation of clouds in a regional model and the impact on the diurnal cycle of convection during Tropical Convection, Cirrus and Nitrogen Oxides (TROCCINOX). *J. Geophys. Res.* **110**: D17103. DOI:10.1029/2004JD005645

Chaboureau JP, Pinty JP. 2006. Validation of a cirrus parameterization with Meteosat Second Generation observations. *Geophys. Res. Lett.* **33**: L03815. DOI:10.1029/2005GL024725

Chaboureau JP, Cammas JP, Mascart P, Pinty JP, Claud C, Roca R, Morcrette JJ. 2000. Evaluation of a cloud system life-cycle simulated by Meso-NH during FASTEX using METEOSAT radiances and TOVS-3I cloud retrievals. *Q. J. R. Meteorol. Soc.* **126**: 1735–1750.

Chaboureau JP, Cammas JP, Mascart P, Pinty JP, Lafore JP. 2002. Mesoscale model cloud scheme assessment using satellite observations. *J. Geophys. Res.* **107**: 4301. DOI:10.1029/2001JD000714

Chaboureau JP, Tulet P, Mari C. 2007. Diurnal cycle of dust and cirrus over West Africa as seen from Meteosat Second Generation satellite and a regional forecast model. *Geophys. Res. Lett.* **34**: L02822. DOI:10.1029/2006GL027771

Chaboureau JP, Söhne N, Pinty JP, Meirold-Mautner I, Defer E, Prigent C, Pardo JR, Mech M, Crewell S. 2008. A midlatitude cloud database validated with satellite observations. *J. Appl. Meteorol. Climatol.* **47**: 1337–1353.

Chiriaco M, Vautard R, Chepfer H, Haeffelin M, Dudhia J, Wanherdrick Y, Morille Y, Protat A. 2006. The ability of MM5 to simulate ice clouds: systematic comparison between simulated and measured fluxes and lidar/radar profiles at the SIRTA atmospheric observatory. *Mon. Weather Rev.* **134**: 897–918.

Collis RT, Russell PB. 1976. *Laser monitoring of the atmosphere*. Springer-Verlag: Berlin.

Cuxart J, Bougeault P, Redelsperger JL. 2000. A turbulence scheme allowing for mesoscale and large-eddy simulations. *Q. J. R. Meteorol. Soc.* **126**: 1–30.

Di Girolamo P, Summa D, Ferretti R. 2009. Rotational Raman Lidar measurements for the characterization of stratosphere–troposphere exchange mechanisms. *J. Atmos. Oceanic Technol.* **26**: 1742–1762.

Dubovik O, Sinyuk A, Lapyonok T, Holben BN, Mishchenko M, Yang P, Eck TF, Volten H, Mu noz O, Veihelmann B, van der Zande WJ, Leon JF, Sorokin M, Slutsker I. 2006. Application of spheroid models to account for aerosol particle nonsphericity in remote sensing of desert dust. *J. Geophys. Res.* **111**: D11208. DOI:10.1029/2005JD006619

Flamant C, Chaboureau JP, Parker DJ, Taylor CM, Cammas JP, Bock O, Timouk F, Pelon J. 2007. Airborne observations of the impact of a convective system on the planetary boundary layer thermodynamics and aerosol distribution in the inter-tropical discontinuity region of the West African Monsoon. *Q. J. R. Meteorol. Soc.* **133**: 1175–1189.

Flamant C, Lavaysse C, Todd M, Chaboureau JP, Pelon J. 2009. Multi-platform observations of a representative springtime case of Bodélé and Sudan dust emission, transport and scavenging over West Africa. *Q. J. R. Meteorol. Soc.* **135**: 413–430.

Fouquart Y, Bonnel B. 1986. Computations of solar heating of the Earth's atmosphere: A new parametrization. *Beitr. Phys. Atmos.* **53**: 35–62.

Gheusi F, Stein J. 2002. Lagrangian description of airflows using Eulerian passive tracers. *Q. J. R. Meteorol. Soc.* **128**: 337–360.

Gregory D, Morcrette JJ, Jakob C, Beljaars AM, Stockdale T. 2000. Revision of convection, radiation and cloud schemes in the ECMWF model. *Q. J. R. Meteorol. Soc.* **126**: 1685–1710.

Grini A, Tulet P, Gomes L. 2006. Dusty weather forecasts using the MesoNH mesoscale atmospheric model. *J. Geophys. Res.* **111**: D19205. DOI:10.1029/2005JD007007

Heinold B, Tegen I, Schepanski K, Hellmuth O. 2008. Dust radiative feedback on Saharan boundary layer dynamics and dust mobilization. *Geophys. Res. Lett.* **35**: L20817. DOI:10.1029/2008GL035319

Kallos G, Papadopoulos A, Katsafados P, Nickovic S. 2006. Transatlantic Saharan dust transport: Model simulation and results. *J. Geophys. Res.* **111**: D09204. DOI:10.1029/2005JD006207

Kishcha P, Barnaba F, Gobbi GP, Alpert P, Shtivelman A, Krichak SO, Joseph JH. 2007. Vertical distribution of Saharan dust over Rome (Italy): Comparison between 3-year model predictions and lidar soundings. *J. Geophys. Res.* **110**: D06208. DOI:10.1029/2006JD007427

Lafore JP, Stein J, Asencio N, Bougeault P, Ducrocq V, Duron J, Fischer C, Héreil P, Mascart P, Masson V, Pinty JP, Redelsperger JL, Richard E, Vilà-Guerau de Arellano J. 1998. The Meso–NH Atmospheric Simulation System. Part I: adiabatic formulation and control simulations. Scientific objectives and experimental design. *Ann. Geophys.* **16**: 90–109.

Meirold-Mautner I, Prigent C, Defer E, Pardo JR, Chaboureau JP, Pinty JP, Mech M, Crewell S. 2007. Radiative transfer simulations using mesoscale cloud model outputs: comparisons with passive microwave and infrared satellite observations for mid-latitudes. *J. Atmos. Sci.* **64**: 1550–1568.

Min QL, Li R, Lin B, Joseph E, Wang S, Hu Y, Morris V, Chang F. 2009. Evidence of mineral dust altering cloud microphysics and precipitation. *Atmos. Chem. Phys.* **9**: 3223–3231.

Mlawer EJ, Taubman SJ, Brown PD, Iacono MJ, Clough SA. 1997. Radiative transfer for inhomogeneous atmospheres: RRTM, a validated corrolated-k model for the longwave. *J. Geophys. Res.* **102**: D16663–16682.

Morcrette JJ, Boucher O, Jones L, Salmond D, Bechtold P, Beljaars A, Benedetti A, Bonet A, Kaiser JW, Razinger M, Schulz M, Serrar S, Simmons AJ, Sofiev M, Suttie M, Tompkins AM, Untch A. 2009. Aerosol analysis and forecast in the European Centre for Medium-Range Weather Forecasts Integrated Forecast System: Forward modeling. *J. Geophys. Res.* **114**: D06206. DOI:10.1029/2008JD011235

Moulin C, Lambert CE, Dayan U, Masson V, Ramonet M, Bousquet P, Legrand M, Balkanski YJ, Guelle W, Marticorena B, Bergametti G, Dulac F. 1998. Satellite climatology of African dust transport in the Mediterranean atmosphere. *J. Geophys. Res.* **103**: D13137–13144.

Müller T, Schladitz A, Massling A, Kaaden N, Kandler K, Wiedensohler A. 2009. Spectral absorption coefficients and imaginary parts of refractive indices of Saharan dust during SAMUM-1. *Tellus* **61B**: 79–95.

Noilhan J, Planton S. 1989. A simple parameterization of land surface processes for meteorological models. *Mon. Weather Rev.* **117**: 536–549.

Papayannis A, Amiridis V, Mona L, Tsaknakis G, Balis D, Bösenberg J, Chaikovski A, De Tomasi F, Grigorov I, Mattis I, Mitev V, Müller D, Nickovic S, Pérez C, Pietruczuk A, Pisani G, Ravetta F, Rizi V, Sicard M, Trickl T, Wiegner M, Gerding M, Mamouri RE, D Amico G, Pappalardo G. 2008. Systematic lidar observations of Saharan dust over Europe in the frame of EARLINET (2000-2002). *J. Geophys. Res.* **113**: D10204. DOI:10.1029/2007JD009028

Pérez C, Nickovic S, Pejanovic G, Baldasano JM, Özsoy E. 2006. Interactive dust-radiation modeling: A step to improve weather forecasts. *J. Geophys. Res.* **111**: D16206. DOI:10.1029/2005JD006717

Pinty JP, Jabouille P. 1998. 'A mixed-phase cloud parameterization for use in a mesoscale non-hydrostatic model: simulations of a squall line and of orographic precipitations'. In *Conf. on Cloud Physics, Everett, WA*. Amer. Meteorol. Soc.: Boston; pp 217–220.

Copyright © 2011 Royal Meteorological Society

Platt CMR. 1973. Lidar and radiometric observations of cirrus clouds. *J. Atmos. Sci.* **30**: 1191–1204.

Richard E, Cosma S, Tabary P, Pinty JP, Hagen M. 2003. High-resolution numerical simulations of the convective system observed in the Lago Maggiore area on 17 September 1999 (MAP IOP 2a). *Q. J. R. Meteorol. Soc.* **129**: 543–563.

Richard E, Chaboureau JP, Flamant C, Champollion C, Hagen M, Schmidt K, Corsmeier U, Barthlott C, Di Girolamo P. 2011. Forecasting summer convection over the Black Forest: a case study from the Convective and Orographically-induced Precipitation Study (COPS) experiment. *Q. J. R. Meteorol. Soc.* **137**(S1): 101–117, DOI: 10.1002/qj.710

Saunders R, Matricardi M, Brunel P, English S, Bauer P, O'Keeffe U, Francis P, Rayer P. 2005. '*RTTOV-8 Science and validation report*', Technical report, NWP SAF Rep., 41 pp.

Schäfler A, Dörnbrack A, Kiemle C, Rahm S, Wirth M. 2010. Tropospheric water vapor transport as determined from airborne lidar measurements. *J. Atmos. Oceanic Technol.* **27**: 2017–2030. DOI:10.1175/2010JTECHA1418.1

Söhne N, Chaboureau JP, Guichard F. 2008. Verification of cloud cover forecast with satellite observation over West Africa. *Mon. Weather Rev.* **136**: 4421–4434.

Stein J, Richard E, Lafore JP, Pinty JP, Asencio N, Cosma S. 2000. High-resolution non-hydrostatic simulations of flash-flood episodes with grid-nesting and ice-phase parameterization. *Meteorol. Atmos. Phys.* **72**: 203–221.

Tegen I, Hoorig P, Chin M, Fung I, Jacob D, Penner J. 1997. Contribution of different aerosol species to the global aerosol extinction optical thickness: Estimates from model results. *J. Geophys. Res.* **102**: 23895–23915.

Torres O, Bhartia PK, Herman JR, Ahmad Z. 1998. Derivation of aerosol properties from satellite measurements of backscattered ultraviolet radiation. Theoretical Basis. *J. Geophys. Res.* **103**: 17099–17110.

Torres O, Bhartia PK, Herman JR, Sinyuk A, Holben B. 2002. A long term record of aerosol optical thickness from TOMS observations and comparison to AERONET measurements. *J. Atmos. Sci.* **59**: 398–413.

Tulet P, Crassier V, Cousin F, Suhre K, Rosset R. 2005. ORILAM, a three-moment lognormal aerosol scheme for mesoscale atmospheric model: Online coupling into the Meso-NH-C model and validation on the Escompte campaign. *J. Geophys. Res.* **110**: D18201. DOI:10.1029/2004JD005716

Tulet P, Mallet M, Pont V, Pelon J, Boone A. 2008. The 7–13 March 2006 dust storm over West Africa: Generation, transport, and vertical stratification. *J. Geophys. Res.* **113**: D00C08. DOI:10.1029/2008JD009871

Wiedner M, Prigent C, Pardo JR, Nuissier O, Chaboureau JP, Pinty JP, Mascart P. 2004. Modeling of passive microwave responses in convective situations using outputs from mesoscale models: comparison with TRMM/TMI satellite observations. *J. Geophys. Res.* **109**: D06214. DOI:10.1029/2003JD004280

Wirth M, Fix A, Mahnke P, Schwarzer H, Schrandt F, Ehret G. 2009. The airborne multi-wavelength water vapor differential absorption lidar WALES: system design and performance. *Appl. Phys. B.* DOI:10.1007/s00340–009–3365–7

Wulfmeyer V, Behrendt A, Bauer HS, Kottmeier C, Corsmeier U, Blyth A, Craig G, Schumann U, Hagen M, Crewell S, Di Girolamo P, Flamant C, Miller M, Montani A, Mobbs S, Richard E, Rotach M, Arpagaus M, Russchenberg H, Schlüssel P, König M, Gärtner V, Steinacker R, Dorninger M, Turner D, Weckwerth T, Hense A, Simmer C. 2008. The Convective and Orographically-induced Precipitation Study (COPS): A Research Project for Improving Quantitative Precipitation Forecasting in Low-mountain Regions. *Bull. Am. Meteorol. Soc.* **89**: 1477–1486.

Yan X, Ducrocq V, Poli P, Hakam M, Jaubert G, Walpersdorf A. 2009. Impact of GPS zenith delay assimilation on convective-scale prediction of Mediterranean heavy rainfall. *J. Geophys. Res.* **114**: D03104. DOI:10.1029/2008JD011036

Zender CS, Bian H, Newman D. 2003. Mineral Dust Entrainment and Deposition (DEAD) model: Description and 1990s dust climatology. *J. Geophys. Res.* **108**: D4416. DOI:10.1029/2002JD002775

Copyright © 2011 Royal Meteorological Society